

Quantifying the redshift space distortion of the bispectrum III : Detection prospects of the multipole moments

Arindam Mazumdar^{1*}, Debanjan Sarkar^{2†}, Somnath Bharadwaj^{1,3‡}

¹Centre for Theoretical Studies, Indian Institute of Technology Kharagpur, Kharagpur - 721302, India

²Department of Physics, Ben-Gurion University of the Negev, Be'er Sheva - 84105, Israel

³Department of Physics, Indian Institute of Technology Kharagpur, Kharagpur - 721302, India

ABSTRACT

The redshift space anisotropy of the bispectrum is generally quantified using multipole moments. The possibility of measuring these multipoles in any survey depends on the level of statistical fluctuations. We present a formalism to compute the statistical fluctuations in the measurement of bispectrum multipoles for galaxy surveys. We consider specifications of a *Euclid* like galaxy survey and present two quantities: the signal-to-noise ratio (SNR) which quantifies the detectability of a multipole, and the rank correlation which quantifies the correlation in measurement errors between any two multipoles. Based on SNR values, we find that *Euclid* can potentially measure the bispectrum multipoles up to $\ell = 4$ across various triangle shapes, formed by the three \mathbf{k} vectors in Fourier space. In general, SNR is maximum for the linear triangles. SNR values also depend on the scales and redshifts of observation. While, $\ell \leq 2$ multipoles can be measured with $\text{SNR} > 5$ even at linear/quasi-linear ($k \lesssim 0.1 \text{ Mpc}^{-1}$) scales, for $\ell > 2$ multipoles, we require to go to small scales or need to increase bin sizes. For most multipole pairs, the errors are only weakly correlated across much of the triangle shapes barring a few in the vicinity of squeezed and stretched triangles. This makes it possible to combine the measurements of different multipoles to increase the effective SNR.

Key words: methods: statistical – cosmology: theory – large-scale structures of Universe.

1 INTRODUCTION

Observations of the Cosmic Microwave Background (CMB) (Fergusson et al. 2012; Oppizzi et al. 2018; Akrami et al. 2020; Shiraishi 2019) and galaxy clustering (Feldman et al. 2001; Scoccimarro et al. 2004; Liguori et al. 2010; Ballardini et al. 2019) indicate that the primordial density fluctuations are consistent with the the simplest models of inflation which predict these to be a Gaussian random field (Baumann 2009). The power spectrum is sufficient to quantify the statistics of a Gaussian random field for which all the higher order statistics are predicted to be zero. However, several inflationary scenarios also predict the primordial fluctuations to be non-Gaussian (primordial non-Gaussianity; Bartolo et al. 2004). Further, the non-linear evolution of initially Gaussian density fluctuations and also the non-linear biasing of the tracer fields (e.g. galaxies) both introduce ‘induced non-Gaussianity’ (Fry 1984; Bernardeau et al. 2002). The bispectrum, which is the Fourier transform of the three-point correlation function, is the lowest order statistics which is sensitive to the non-Gaussianity. Second order perturbation theory predicts that measurements of the bispectrum in the weakly non-linear regime can be used to constrain the bias parameters (Matarrese et al. 1997), and this framework has been applied in

several galaxy surveys to extract the galaxy bias parameters (Feldman et al. 2001; Scoccimarro et al. 2001; Verde et al. 2002; Nishimichi et al. 2007; Gil-Marín et al. 2015). Further, measurements of the bispectrum allow us to break the degeneracy between the matter density parameter Ω_m and the linear bias parameter b_1 , something which is not possible by using the power spectrum alone (Scoccimarro et al. 1999). A precise measurement of the Baryon Acoustic Oscillations (BAO) in the bispectrum allows us to constrain the expansion rate of the universe Pearson & Samushia (2018). Upcoming galaxy surveys like *Euclid* (Blanchard et al. 2020), promises to measure the bispectrum with high precision, and thereby constrain the above parameters with unprecedented accuracy.

Redshift space distortion (RSD) is an important effect in galaxy redshift surveys (Kaiser 1987; Jackson 1972; Hamilton 1998). The line-of-sight (LoS) anisotropy in the redshift space power spectrum contains a wealth of cosmological information. For example, this can be used to: (i) measure the growth of structures f on linear scales (Loveday et al. 1996; Peacock et al. 2001; Hawkins et al. 2003; Guzzo et al. 2008), (ii) constrain the total density from massive neutrinos (Hu et al. 1998; Upadhye 2019), and (iii) test dark energy and modified gravity theories (Linder 2008; Song & Percival 2009; de la Torre et al. 2017; Johnson et al. 2016; Mueller et al. 2018).

The bispectrum also is affected by RSD, and the redshift space bispectrum also contains a wealth of cosmological in-

* arindam.mazumdar@iitkgp.ac.in

† debanjan@post.bgu.ac.il

‡ somnath@phy.iitkgp.ac.in

formation (Scoccimarro et al. 1999; Yankelevich & Porciani 2019; Hahn & Villaescusa-Navarro 2021), and it is important to accurately model and quantify this. Hivon et al. (1995) and Verde et al. (1998) have formulated the initial theoretical framework for calculating the bispectrum in redshift space. However, they mainly focused on measuring the large scale bias parameter and the cosmological parameters, and they have not quantified the RSD anisotropy in general. Later, Scoccimarro et al. (1999) have quantified the anisotropy of the redshift space bispectrum utilizing spherical harmonics. Their work, however, was restricted only to the monopole and one quadrupole component ($\ell = 2, m = 0$). The work of Hashimoto et al. (2017) also was limited to a single quadrupole component of the redshift space bispectrum. Nan et al. (2018) have calculated approximate analytical expressions for the higher angular multipole moments up to $\ell = 4$ based on the halo model, and their analysis is only limited to a few triangle configurations. Yankelevich & Porciani (2019) and Gualdi & Verde (2020) have analysed the combined ability of the redshift space power spectrum and bispectrum to constrain the cosmological parameters. Desjacques et al. (2018) have utilised effective field theory to model the redshift space bispectrum on quasi non-linear scales. The theoretical analysis of Clarkson et al. 2019 and de Weerd et al. (2020) suggests that relativistic effects will introduce a dipole anisotropy in the redshift space bispectrum on very large length-scales.

There has been some work towards developing fast estimators which quantify the anisotropy of the redshift space bispectrum. Slepian & Eisenstein (2017); Slepian & Eisenstein (2018) have introduced a technique to expand the redshift space three-point correlation function in terms of the products of two spherical harmonics. On the other hand, Sugiyama et al. (2019) have proposed a tri-polar spherical harmonic decomposition to quantify the anisotropy of the redshift space bispectrum, and as a demonstration they applied this to the Baryon Oscillation Spectroscopic Survey (BOSS) Data Release 12.

Our recent work (Bharadwaj et al. 2020, hereafter Paper I) presents a formalism to quantify the anisotropy of the redshift space bispectrum $B^s(\mathbf{k}_a, \mathbf{k}_b, \mathbf{k}_c)$ by decomposing it into multipole moments $\bar{B}_\ell^m(k_1, \mu, t)$. Here k_1 , the length of the largest side, and (μ, t) respectively quantify the size and shape of the triangle $(\mathbf{k}_a, \mathbf{k}_b, \mathbf{k}_c)$. We have illustrated this formalism by quantifying the anisotropy due to linear RSD of the bispectrum arising from primordial non-Gaussianity. We have found that only the first four even ℓ multipoles are non-zero, for which we have presented explicit analytical expressions. These results are expected to be important to constrain f_{NL} using the bispectrum measured from future redshift surveys. In a subsequent work Mazumdar et al. (2020) (hereafter Paper II), the same formalism was used to quantify the anisotropy of the induced redshift space bispectrum arising from Gaussian initial conditions. We present analytical expressions for all the multipole moments which are predicted to be non-zero ($\ell \leq 8, m \leq 6$) at second order perturbation theory. Considering triangles of all possible shapes, we have analysed the shape dependence of all the multipoles holding $k_1 = 0.2 \text{ Mpc}^{-1}, \beta_1 = 1, b_1 = 1$ and $\gamma_2 = 0$ fixed. Here β_1, b_1 and γ_2 , quantify the linear redshift distortion parameter, linear bias and quadratic bias respectively. For most multipoles we find that the maxima or minima, or both, occur very close

to the squeezed limit. Further, the absolute values $|\bar{B}_\ell^m|$ are found to decrease rapidly if either ℓ or m are increased. We have also provided rough estimates for measuring the various multipoles using upcoming galaxy redshift surveys. The present paper presents a detailed analysis for the prospects of measuring the various multipole moments using upcoming galaxy redshift surveys.

The ability to measure any particular bispectrum multipole \bar{B}_ℓ^m primarily depends on its amplitude, the galaxy number density and the extent of the survey volume. Until recently, measurements of the bispectrum were limited by the shot noise from the limited galaxy number density and the cosmic variance due to the limited volume of the galaxy redshift surveys (Scoccimarro et al. 2001; Verde et al. 2002; Croton et al. 2004; Jing & Boerner 2004; Kulkarni et al. 2007; Gaztanaga et al. 2009; Marin 2011). However, Gil-Marín et al. (2015, 2017); Philcox & Ivanov (2022) have recently measured the isotropic component (monopole) of the galaxy bispectrum using the Baryon Oscillation Spectroscopic Survey at a relatively high level of precision. They showed that it is possible to improve the constraints on the cosmological parameters by including the bispectrum along with the power spectrum. Upcoming galaxy surveys will cover unprecedented large volumes with high galaxy number density, and it is anticipated that this will enable us to precisely measure the higher multipoles of the bispectrum. For example, the *Euclid* space telescope (Blanchard et al. 2020) is expected to complete a wide survey that will measure $\sim 10^8$ galaxy redshifts over 15,000 square degrees on the sky in the range $z \lesssim 2.5$. Precise measurements of the galaxy bispectrum using *Euclid* are expected to place tight constraints on: (i) primordial non-Gaussianity (Fedeli et al. 2011; Dai & Xia 2020), (ii) neutrino masses (Chudaykin & Ivanov 2019; Hahn & Villaescusa-Navarro 2021), (iii) modified gravity models (Bose et al. 2020), and (iv) all the other currently constrained standard cosmological parameters (Agarwal et al. 2021). The above estimates mostly rely on the real-space bispectrum or its redshift space monopole. It is important and interesting to also consider the higher multipoles of the bispectrum in order to utilize the full reach of this mission (Gualdi & Verde 2020).

In this paper we developed a formalism to calculate the statistical fluctuations expected in the bispectrum multipoles measured from any given galaxy redshift survey. We quantify these statistical fluctuations through the error covariance of the different multipoles. Here we have considered the specifications of the *Euclid* galaxy redshift survey for which we present the signal-to-noise ratio (SNR) with which the different multipoles are expected to be measured. We also present results for the correlations expected between the different multipole moments. The paper is organised as follows. In Section 2, we present the formalism for calculating the error covariance between different bispectrum multipoles. In Section 3 we present our main results, which include the dependence of bispectrum multipoles on triangle shapes, sizes and redshifts, possibility of measuring the different multipoles, and error covariance between the pair of multipoles in terms of rank correlation. Finally in Section 4, we summarize our findings and outline some future directions. In this paper, we use the *Boltzmann* code CLASS (Lesgourgues 2011; Blas et al. 2011) to calculate the input matter power spectrum for our analysis and assumed cosmological param-

eters from Planck 2015 (Planck Collaboration et al. 2016) throughout the work.

2 FORMALISM

We first consider $\delta^s(\mathbf{x})$ which represents the density contrast of a smooth cosmological field in redshift space. This can be decomposed into Fourier modes using

$$\delta^s(\mathbf{x}) = \frac{1}{V} \sum_{\mathbf{k}} e^{i\mathbf{k}\cdot\mathbf{x}} \Delta^s(\mathbf{k}), \quad (1)$$

for which, in the absence of Poisson noise, the power spectrum is defined as

$$\langle \Delta^s(\mathbf{k}_1) \Delta^s(\mathbf{k}_2) \rangle = V \delta_{\mathbf{k}_1+\mathbf{k}_2,0} P^s(k_1, \mu_1), \quad (2)$$

where μ_1 is the cosine of the angle between the Fourier mode \mathbf{k}_1 and the line of sight (LoS) direction $\hat{\mathbf{n}}$. We have considered $\hat{\mathbf{n}} = \hat{\mathbf{z}}$ here. The bispectrum is similarly defined as

$$\langle \Delta^s(\mathbf{k}_1) \Delta^s(\mathbf{k}_2) \Delta^s(\mathbf{k}_3) \rangle = V \delta_{\mathbf{k}_1+\mathbf{k}_2+\mathbf{k}_3,0} B^s(\mathbf{k}_1, \mathbf{k}_2, \mathbf{k}_3). \quad (3)$$

Throughout this paper we assume that the three vectors ($\mathbf{k}_a, \mathbf{k}_b, \mathbf{k}_c$), which form a closed triangle, are ordered such that $k_1 \geq k_2 \geq k_3$. In the absence of redshift space distortion the bispectrum depends only on the shape and size of the triangle formed by the three vectors ($\mathbf{k}_1, \mathbf{k}_2, \mathbf{k}_3$). Here, following Paper I, we parametrize this using (k_1, μ, t) where k_1 the length of the largest edge quantifies the size of the triangle while $\mu = \cos \theta$ (fig. 1) and $t = k_2/k_1$ together quantify the shape of the triangle. Note that μ and t are both bounded within the range $0.5 \leq \mu, t \leq 1$ and $2\mu t \geq 1$. In the presence of redshift space distortion the bispectrum also depends on $\mu_a = \mathbf{k}_a \cdot \hat{\mathbf{n}}/k_a$ where $a = 1, 2, 3$. Therefore, the bispectrum now depends on how the triangle is oriented with respect to $\hat{\mathbf{n}}$.

It is necessary to consider triangles of all possible orientations in order to quantify the anisotropy of the redshift space bispectrum. Here we start from a reference triangle in the $x-z$ plane (fig. 1) for which we have

$$\begin{aligned} \mathbf{k}_1 &= k_1 \hat{\mathbf{z}}, \\ \mathbf{k}_2 &= k_1 t [-\mu \hat{\mathbf{z}} + \sqrt{1-\mu^2} \hat{\mathbf{x}}], \end{aligned} \quad (4)$$

and $\mathbf{k}_3 = -\mathbf{k}_1 - \mathbf{k}_2$. It is possible to obtain all possible orientations of the triangle by applying different rotations $\hat{\mathcal{R}}$ to the reference triangle. We parameterize these rotations using (α, β, γ) the Euler angles which refer to successive rotations along the z, y and z axes respectively (Sakurai 1994). We then have

$$\begin{aligned} \mu_1 &= p_z \\ \mu_2 &= -\mu p_z + \sqrt{1-\mu^2} p_x \\ \mu_3 &= \frac{-[(1-\mu t)p_z + t\sqrt{1-\mu^2} p_x]}{\sqrt{1-2\mu t + t^2}} \end{aligned} \quad (5)$$

where we have introduced a unit vector $\hat{\mathbf{p}} = \hat{\mathcal{R}}^{-1} \hat{\mathbf{n}}$ which has components $p_z = \cos(\beta)$ and $p_x = -\sin(\beta) \cos(\gamma)$ respectively. Note that these expressions are independent of α *i.e.* the axis of the first rotation (z) coincides with $\hat{\mathbf{n}}$, and it does not affect the redshift space distortion. In summary, the redshift space bispectrum $B^s(\mathbf{k}_1, \mathbf{k}_2, \mathbf{k}_3)$ can be completely parameterized using $B^s(k_1, \mu, t, \hat{\mathbf{p}})$ where (k_1, μ, t) quantify

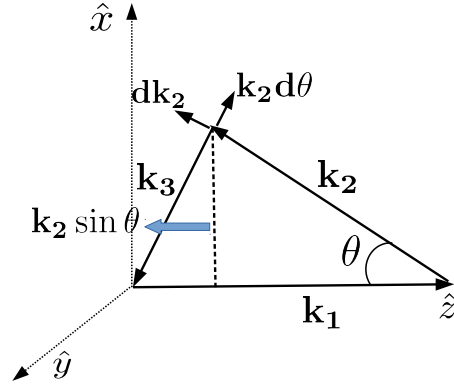


Figure 1. This shows a reference triangle ($\mathbf{k}_1, \mathbf{k}_2, \mathbf{k}_3$) in $x-z$ plane which is used to define various parameters used here. $d\mathbf{k}_2, d\theta$ represents the binning of the bi-spectrum triangle discussed in Section 2.3.

the size and shape dependence of the triangle while $\hat{\mathbf{p}}$ quantifies its orientation with respect to $\hat{\mathbf{n}}$.

The redshift space anisotropy of the bispectrum is quantified using multipole moments defined as

$$\bar{B}_\ell^m(k_1, \mu, t) = \sqrt{\frac{2\ell+1}{4\pi}} \int [Y_\ell^m(\hat{\mathbf{p}})]^* B^s(k_1, \mu, t, \hat{\mathbf{p}}) d\Omega_{\hat{\mathbf{p}}} \quad (6)$$

where the integral over the solid angle $d\Omega_{\hat{\mathbf{p}}}$ accounts for all possible orientations of the triangle. As discussed in Paper I, only the even ℓ multipoles of the bispectrum are non-zero and these are all real valued.

In reality, we encounter a finite number of Fourier modes distributed on a regular grid. Here we define the bispectrum multipole estimator as a discrete sum over triangle configurations in Fourier space,

$$\hat{B}_\ell^m(k_1, \mu, t) = \sum_n \frac{w_\ell^m(\hat{\mathbf{p}}_n)}{2V} [\Delta^s(\mathbf{k}_n) \Delta^s(\bar{\mathbf{k}}_n) \Delta^s(\tilde{\mathbf{k}}_n) + c.c.] \quad (7)$$

where $\mathbf{k}_n + \bar{\mathbf{k}}_n + \tilde{\mathbf{k}}_n = 0$ form a closed triangle, each value of n represents a different closed triangle, *c.c.* \equiv complex conjugate, and

$$w_\ell^m(n) = \text{Re} \left[\sqrt{\frac{2\ell+1}{4\pi}} \frac{Y_\ell^m(\hat{\mathbf{p}}_n)}{\sum_{n_1} |Y_\ell^m(\hat{\mathbf{p}}_{n_1})|^2} \right]. \quad (8)$$

The sum over n covers triangles of all possible orientations, with shape and size in a bin of extent $(\Delta k_1, \Delta \mu, \Delta t)$ around (k_1, μ, t) . The exact binning scheme used for the present work is discussed later in this paper.

2.1 The Error Covariance

We assume that the grid spacing in \mathbf{k} is adequately fine so that various triangle orientations are adequately sampled which implies that $\langle \hat{B}_\ell^m(k_1, \mu, t) \rangle = \bar{B}_\ell^m(k_1, \mu, t)$ where $\langle \dots \rangle$ denotes an ensemble average of different realisations of the random density field $\Delta(\mathbf{k})$. In the present work we are interested in the statistical fluctuations (error)

$$\Delta \hat{B}_\ell^m = \hat{B}_\ell^m(k_1, \mu, t) - \bar{B}_\ell^m(k_1, \mu, t) \quad (9)$$

which we quantify through the covariance

$$C_{\ell\ell'}^{mm'} = \langle \Delta \hat{B}_\ell^m \Delta \hat{B}_{\ell'}^{m'} \rangle. \quad (10)$$

We calculate this using

$$\begin{aligned} C_{\ell\ell'}^{mm'} + \bar{B}_\ell^m \bar{B}_{\ell'}^{m'} &= (2V)^{-2} \sum_{n_1, n_2} w_\ell^m(\hat{\mathbf{p}}_{n_1}) w_{\ell'}^{m'}(\hat{\mathbf{p}}_{n_2}) \times \\ &[\langle \Delta^s(\mathbf{k}_{n_1}) \Delta^s(\bar{\mathbf{k}}_{n_1}) \Delta^s(\tilde{\mathbf{k}}_{n_1}) \Delta^s(\mathbf{k}_{n_2}) \Delta^s(\bar{\mathbf{k}}_{n_2}) \Delta^s(\tilde{\mathbf{k}}_{n_2}) \rangle + \\ &c.c. + \\ &\langle \Delta^s(\mathbf{k}_{n_1}) \Delta^s(\bar{\mathbf{k}}_{n_1}) \Delta^s(\tilde{\mathbf{k}}_{n_1}) \Delta^{s*}(\mathbf{k}_{n_2}) \Delta^{s*}(\bar{\mathbf{k}}_{n_2}) \Delta^{s*}(\tilde{\mathbf{k}}_{n_2}) \rangle \\ &+ c.c.]. \end{aligned} \quad (11)$$

We have evaluated this using

$$\begin{aligned} &\langle \Delta^s(\mathbf{k}_{n_1}) \Delta^s(\bar{\mathbf{k}}_{n_1}) \Delta^s(\tilde{\mathbf{k}}_{n_1}) \Delta^s(\mathbf{k}_{n_2}) \Delta^s(\bar{\mathbf{k}}_{n_2}) \Delta^s(\tilde{\mathbf{k}}_{n_2}) \rangle = \\ &[1 + 3\delta_{n_1, n_2}] V^2 B^s(\mathbf{k}_{n_1}, \bar{\mathbf{k}}_{n_1}, \tilde{\mathbf{k}}_{n_1}) B^s(\mathbf{k}_{n_2}, \bar{\mathbf{k}}_{n_2}, \tilde{\mathbf{k}}_{n_2}) \\ &+ \delta_{n_1, -n_2} V^3 P^s(\mathbf{k}_{n_1}) P^s(\bar{\mathbf{k}}_{n_1}) P^s(\tilde{\mathbf{k}}_{n_1}) \end{aligned} \quad (12)$$

which assumes that the signal is weakly non-Gaussian whereby contributions from T^s the trispectrum and P_6^s the sixth order polyspectrum can be neglected. Here δ_{n_1, n_2} is a Kronecker delta which has value one only when n_1 and n_2 refer to the same triangle and is zero otherwise. Further, $-n_2$ refers to the same triangle as n_2 , but the two are exactly oppositely oriented *i.e.* $\mathbf{k}_{-n_1} = -\mathbf{k}_{n_1}$, etc. Also note that $\Delta^s(\mathbf{k}_{-n_2}) = \Delta^{s*}(\mathbf{k}_{n_2})$. Using these in eq. (10) we obtain

$$\begin{aligned} C_{\ell\ell'}^{mm'} &= \sum_n w_\ell^m(\hat{\mathbf{p}}_n) w_{\ell'}^{m'}(\hat{\mathbf{p}}_n) \times \\ &\{3[B^s(\mathbf{k}_n, \bar{\mathbf{k}}_n, \tilde{\mathbf{k}}_n)]^2 + V P^s(\mathbf{k}_n) P^s(\bar{\mathbf{k}}_n) P^s(\tilde{\mathbf{k}}_n)\} \end{aligned} \quad (13)$$

which provides an estimate of the error covariance in the absence of Poisson noise.

2.2 Poisson noise

We now consider a discrete tracer (*e.g.* galaxies) whose density represents a Poisson sampling of the smooth field which we have been discussing till now. We use $\Delta_g(\mathbf{k})$ to represent the corresponding density contrast in Fourier space. The discrete sampling of the smooth field gives rise to a shot noise (or Poisson noise) whose contribution to the power spectrum and the bi-spectrum are well studied (Peebles 1980; Scoccimarro et al. 2001; Smith 2009). Using $\Delta_g(\mathbf{k})$ instead of $\Delta(\mathbf{k})$ in eq. (2) to estimate the power spectrum, we have

$$V^{-1} \langle \Delta_g^s(\mathbf{k}_1) \Delta_g^{s*}(\mathbf{k}_1) \rangle = P^s(k_1, \mu_1) + n_g^{-1}, \quad (14)$$

where, $P^s(k_a, \mu_a)$ is the power spectrum of the smooth field $\Delta(\mathbf{k})$ and n_g is the number density of galaxies. Similarly considering the bispectrum we have

$$\begin{aligned} V^{-1} \langle \Delta_g^s(\mathbf{k}_1) \Delta_g^s(\mathbf{k}_1) \Delta_g^s(\mathbf{k}_3) \rangle &= B^s(\mathbf{k}_1, \mathbf{k}_2, \mathbf{k}_3) + \\ n_g^{-1} [P^s(k_1, \mu_1) + P^s(k_2, \mu_2) + P^s(k_3, \mu_3)] &+ n_g^{-2} \end{aligned} \quad (15)$$

where it has been assumed that $\mathbf{k}_1 + \mathbf{k}_2 + \mathbf{k}_3 = 0$. It is now necessary to consider how eq. (13) for the bispectrum error covariance is modified if we account for the discrete sampling. We first consider the ensemble average of the product of six $\Delta_g(\mathbf{k})$ s which is required to calculate the covariance (eq. 10). Here we use the shortened notation $\Delta_{ag} \equiv \Delta_g(\mathbf{k}_a)$, $\Delta_a \equiv \Delta(\mathbf{k}_a)$, $\Delta_{ab} \equiv \Delta(\mathbf{k}_a + \mathbf{k}_b)$, $\Delta_{abc} \equiv \Delta(\mathbf{k}_a + \mathbf{k}_b + \mathbf{k}_c)$,

etc. We then have

$$\begin{aligned} &\langle [\Delta_{ag} \Delta_{bg} \Delta_{cg} \Delta_{dg} \Delta_{eg} \Delta_{fg}] - [\Delta_a \Delta_b \Delta_c \Delta_d \Delta_e \Delta_f] \rangle = \\ &V n_g^{-5} + n_g^{-4} \langle [\Delta_a \Delta_{bcdef} + \Delta_{ab} \Delta_{cdef} + \Delta_{abc} \Delta_{cdef}] \rangle + \\ &n_g^{-3} \langle [\Delta_a \Delta_b \Delta_{cdef} + \Delta_a \Delta_{bc} \Delta_{def} + \Delta_{ab} \Delta_{cd} \Delta_{ef}] \rangle + \\ &n_g^{-2} \langle [\Delta_a \Delta_b \Delta_c \Delta_{def} + \Delta_a \Delta_b \Delta_{cd} \Delta_{ef}] \rangle \\ &n_g^{-1} \langle [\Delta_a \Delta_b \Delta_c \Delta_d \Delta_{ef}] \rangle + \text{combinations} \end{aligned} \quad (16)$$

where all the terms in the *r.h.s.* arise due to the discrete sampling, and for each term it is necessary to also consider all the distinct combinations of the indices a, b, c, \dots . Instead of embarking on a detailed calculation of the *r.h.s.*, we present it in a schematic form which can be used for an order of magnitude estimate. Using $[C_{\ell\ell'}^{mm'}]_g$ and $C_{\ell\ell'}^{mm'}$ to represent the error covariance respectively in the presence and absence of shot noise, we have

$$\begin{aligned} [C_{\ell\ell'}^{mm'}]_g - C_{\ell\ell'}^{mm'} &\sim V^{-1} [n_g^{-5} + n_g^{-4} P^s + n_g^{-3} B^s] \\ &+ n_g^{-2} [P^s]^2 + n_g^{-1} P^s B^s \end{aligned} \quad (17)$$

where $C_{\ell\ell'}^{mm'} \sim V [P^s]^3 + 3 [B^s]^2$ (eq. 13). Here we consider estimates for the upcoming *Euclid* survey (Laureijs et al. 2011) which is expected to cover $V \sim 10^9 \text{ Mpc}^3$. Following Yankelevich & Porciani (2019) we adopt $n_g \sim 10^{-3} \text{ Mpc}^{-3}$ and a linear bias parameter $b \sim 1$ at $z = 0.7$. We have used Blas et al. (2011) to estimate $P^s \sim 10^4 \text{ Mpc}^3$ and $B^s \sim [P^s]^2$ at $k \sim 0.2 \text{ Mpc}^{-1}$ where we expect second order perturbation to be reasonably valid. Using these, we first consider eq. (14) where we have $P^s \sim 10^4 \text{ Mpc}^3$ and $n_g^{-1} \sim 10^3 \text{ Mpc}^3$. Similarly in eq. (15) we have $B^s \sim 10^8 \text{ Mpc}^6$, whereas $n_g^{-1} P^s \sim 10^7 \text{ Mpc}^6$ and $n_g^{-2} \sim 10^6 \text{ Mpc}^6$. These estimates show that it is necessary to account for the shot noise in order to correctly estimate the power spectrum and the bispectrum. We now consider the error covariance for which we have $V [P^s]^3 \sim 10^{21} \text{ Mpc}^{12}$ and $[B^s]^2 \sim 10^{16} \text{ Mpc}^{12}$ whereby $C_{\ell\ell'}^{mm'} \sim 10^{21} \text{ Mpc}^{12}$ *i.e.* the error in the estimated bispectrum is dominated by the terms $\sim V [P^s]^3$. Considering the shot noise, we see that we have the largest contribution from $n_g^{-1} P^s B^s \sim 10^{15} \text{ Mpc}^{12}$ and the magnitude decreases with increasing power of n_g^{-1} with the smallest contribution coming from $V^{-1} n_g^{-5} \sim 10^6 \text{ Mpc}^{12}$. Even if we consider a lower galaxy number density $n_g \sim 10^{-4} \text{ Mpc}^{-3}$, we find that the terms $V^{-1} [\dots]$ are all $\sim 10^{11} \text{ Mpc}^{12}$ and the two remaining terms are $\sim 10^{16} \text{ Mpc}^{12}$, all of which are several orders of magnitude smaller than the predicted value of $C_{\ell\ell'}^{mm'}$. We conclude that it is quite reasonable to ignore the shot noise contribution, and we use $C_{\ell\ell'}^{mm'}$ for the error estimates presented in the subsequent analysis.

2.3 Binning

We finally discuss the binning scheme which we have considered here. For the purpose of analytic predictions, it is convenient to assume that V is very large whereby dN_k the number of \mathbf{k} modes in the interval d^3k is given by $dN_k = (2\pi)^{-3} V d^3k$. The number of triangles dN_{tr} is then given by

$$dN_{tr} = (2\pi)^{-6} V^2 d^3k_1^3 d^3k_2^3, \quad (18)$$

and we replace the sum in eq. (13) using $\sum_n \rightarrow \int dN_{tr}$. Starting from $\mathbf{k}_1 = k_1 \hat{x}$ (fig. 1) we obtain all other possible vectors \mathbf{k}_1 by changing the length k_1 or rotations through

the Euler angles α and β , and we have

$$d^3 k_1 = k_1^2 dk_1 d\beta \sin \beta d\alpha. \quad (19)$$

Considering \mathbf{k}_2 , a change in length could occur through either a change in k_1 or in t , whereas a change in orientation is associated with either a change in $\mu = \cos \theta$ or γ the third Euler angle. We then have

$$d^3 k_2 = k_1^2 t^2 (t dk_1 + k_1 dt) d\mu d\gamma. \quad (20)$$

Here we have considered bins of extent $(\Delta k_1, \Delta \mu, \Delta t)$ centered around (k_1, μ, t) . Using eq. (19) and eq. (20), we have

$$dN_{tr} = (8\pi^2)^{-1} N_{tr} d\alpha \sin \beta d\beta d\gamma \quad (21)$$

where N_{tr} the number of triangles in any particular bin is given by

$$N_{tr} = (8\pi^4)^{-1} (V k_1^3)^2 t^2 [\Delta \ln k_1 (t \Delta \ln k_1 + \Delta t) \Delta \mu] \quad (22)$$

Using these we have

$$\sum_{n_1} |Y_\ell^m(\hat{\mathbf{p}}_{n_1})|^2 = (4\pi)^{-1} N_{tr} \quad (23)$$

which we use in the expression for w_ℓ^m (eq. 8) to write eq. (13) as

$$\begin{aligned} C_{\ell\ell'}^{mm'}(k_1, \mu, t) &= \frac{\sqrt{(2\ell+1)(2\ell'+1)}}{N_{tr}} \int d\Omega_{\hat{\mathbf{p}}} \times \\ & \text{Re}[Y_\ell^m(\hat{\mathbf{p}})] \text{Re}[Y_{\ell'}^m(\hat{\mathbf{p}})] \left\{ 3[B^s(k_1, \mu, t, \hat{\mathbf{p}})]^2 \right. \\ & \left. + VP^s(k_1, \mu_1)P^s(k_2, \mu_2)P^s(k_3, \mu_3) \right\} \end{aligned} \quad (24)$$

Note that $k_2, k_3, \mu_1, \mu_2, \mu_3$ can all be calculated from $(k_1, \mu, t, \hat{\mathbf{p}})$ using eq. (4) and eq. (5). We have used eq. (24) to calculate the error estimates presented subsequently in this paper considering bins of extent $(\Delta \ln k_1 = 0.1, \Delta \mu = 0.05, \Delta t = 0.05)$.

2.4 Second Order Induced Bispectrum

The induced bispectrum for any tracer in redshift space from second-order perturbation theory (2LPT) can be written as

$$\begin{aligned} B_{2PT}^s(\mathbf{k}_1, \mathbf{k}_2, \mathbf{k}_3) &= 2b_1^{-1}(1 + \beta_1 \mu_1^2)(1 + \beta_1 \mu_2^2) \left\{ F_2(\mathbf{k}_1, \mathbf{k}_2) \right. \\ & + \frac{\gamma_2}{2} + \mu_3^2 \beta_1 G_2(\mathbf{k}_1, \mathbf{k}_2) \\ & - b_1 \beta_1 \mu_3 k_3 \left[\frac{\mu_1}{k_1} (1 + \beta_1 \mu_2^2) \right. \\ & \left. \left. + \frac{\mu_2}{k_2} (1 + \beta_1 \mu_1^2) \right] \right\} P(k_1)P(k_2) + \text{cyc} \dots, \end{aligned} \quad (25)$$

where β_1 is the linear redshift distortion parameter, $\gamma_2 = b_2/b_1$ where b_1 is the linear bias and b_2 is the quadratic bias, and

$$G_2(k_1, k_2) = \frac{3}{7} + \frac{\mathbf{k}_1 \cdot \mathbf{k}_2}{2} \left(\frac{1}{k_1^2} + \frac{1}{k_2^2} \right) + \frac{4}{7} \frac{(\mathbf{k}_1 \cdot \mathbf{k}_2)^2}{k_1^2 k_2^2}, \quad (26)$$

refers to the second order kernel for the divergence of the peculiar velocity. Here we find it convenient to use the following notation

$$F_2(\mathbf{k}_1, \mathbf{k}_2) = G_2(\mathbf{k}_1, \mathbf{k}_2) + \Delta G(\mathbf{k}_1, \mathbf{k}_2) \quad (27)$$

where

$$\Delta G(\mathbf{k}_1, \mathbf{k}_2) = \frac{2}{7} \left[1 - \frac{(\mathbf{k}_1 \cdot \mathbf{k}_2)^2}{k_1^2 k_2^2} \right]. \quad (28)$$

Note that, the notations used here are taken explicitly from [Paper I](#) and [Paper II](#).

In [Paper II](#), we have quantified the anisotropy of the induced redshift-space 2LPT bispectrum (eq. 25) in terms of the multipole moments $\bar{B}_\ell^m(k_1, \mu, t)$ defined in eq. (6). There we have also presented the formulas needed to calculate all the multipole moments that are predicted to be non-zero at second-order perturbation theory. Further, we have analysed the $\mu - t$ dependence of $\bar{B}_\ell^m(k_1, \mu, t)$ at fixed $k_1 = 0.2 \text{ Mpc}^{-1}$ and for the parameter values $\beta_1 = 1, b_1 = 1, \gamma_2 = 0$. We find that the even multipole moments \bar{B}_0^0, \bar{B}_2^0 and \bar{B}_4^0 show very similar behaviour where their values are positive in the whole $\mu - t$ plane, the smallest values occur near the equilateral triangles and the largest values are found for the linear triangles. Two other even multipole moments \bar{B}_2^2 and \bar{B}_4^4 show positive values in the whole $\mu - t$ plane, however, their shape dependence is different from the multipoles discussed above. For the rest of the multipole moments, we find that they exhibit negative values at some parts of or through the entire $\mu - t$ plane. Their contour patterns are also different from each other. We broadly see that, although the higher multipoles ($\ell > 2$) show rich variety of shape dependence, their amplitude $|\bar{B}_\ell^m|$ fall off sharply as ℓ and m are increased. Note that, the analysis in [Paper II](#) ignores the Finger-of-God (FoG) effect. At large scales linear perturbation theory and its second order extension are expected to provide a reasonably accurate description of the clustering of matter in real space. This however does not hold in redshift space where it is found that large peculiar velocities arising from highly non-linear small scale structures cause the large scale clustering pattern to appear elongated along the LoS. This is known as the Finger of God (FoG) effect, and it is important to include this in any realistic analysis of the redshift space power spectrum and bispectrum.

2.5 Finger of God Effect

In case of the power spectrum, the FoG effect is generally incorporated as an ad-hoc damping profile which multiplies the linear redshift space power spectrum. A number of profiles, namely Lorentzian, Gaussian, Lorentzian-squared *etc.*, have been considered in the literature. Although the Lorentzian profile works well for the simulated data ([Davis & Peebles 1982](#); [Hamilton 1997](#); [Hatton & Cole 1999](#); [Seljak 2001](#); [White 2001](#); [Sarkar & Bharadwaj 2018, 2019](#)), the Gaussian profile is expected to occur naturally ([Bharadwaj 2001](#); [Scoccimarro 2004](#); [Hikage & Yamamoto 2013](#); [Hikage et al. 2013](#); [Okumura et al. 2015](#); [Hikage & Yamamoto 2016](#)). In this work, we consider a Gaussian profile for the FoG damping and model the FoG redshift-space power spectrum as ([Peacock 1992](#))

$$P_{\text{FoG}}^s(k_1, \mu_1) = \exp \left[(-k_1^2 \mu_1^2) \frac{\sigma_p^2}{2} \right] \times P_{\text{1PT}}^s(k_1, \mu_1) \quad (29)$$

where $P_{\text{1PT}}^s(k_1, \mu_1) = (1 + \beta_1 \mu_1^2)^2 P(k_1)$ is the linear redshift space power spectrum, and σ_p parametrizes the pairwise velocity dispersion in units of comoving Mpc. We can equivalently use $[\sigma_p a H(a)]$ in units of km s^{-1} . Note that on very large scales $k_1 \sigma_p \ll 1$, the damping factor

$\exp[-k_1^2\mu_1^2\sigma_p^2/2] \approx 1$, and the Kaiser effect $(1 + \beta_1\mu_1^2)^2$ suffices to describe the RSD effect.

We similarly incorporate the FoG effect for the bispectrum as

$$B_{\text{FoG}}^s(\mathbf{k}_1, \mathbf{k}_2, \mathbf{k}_3) = \exp\left[-(k_1^2\mu_1^2 + k_2^2\mu_2^2 + k_3^2\mu_3^2)\frac{\sigma_p^2}{2}\right] \times B_{2\text{PT}}^s(\mathbf{k}_1, \mathbf{k}_2, \mathbf{k}_3) \quad (30)$$

where we use eq. (25) to calculate $B_{2\text{PT}}$. Due to the FoG damping term, we do not have closed form analytic expressions for the various multipole moments of B_{FoG}^s . Here we have numerically integrated eq. (6) to compute the various multipole moments for which the results are presented in the following section.

3 RESULTS

In this section we present the shape and size dependence of the redshift space bispectrum, and also the corresponding statistical errors for an *Euclid* like survey. As discussed in Section 2, we have used the largest side k_1 to quantify the size of the triangle, and we have used $\mu = \cos\theta$ and $t = k_2/k_1$ (fig. 1) to quantify the shape. Following Fry (1984), we have defined the dimensionless bispectrum multipoles (Paper II)

$$Q_\ell^m(k_1, \mu, t) = b_1 \frac{\bar{B}_\ell^m(k_1, \mu, t)}{3P(k_1)^2}, \quad (31)$$

which we have used to exhibit the results presented here.

Galaxy surveys like *Euclid* expect to cover a broad redshifts range from 0.001 to 2.5 (Ilić et al. 2021; Pozzetti et al. 2016), which can be divided into various redshift bins for the subsequent analysis. For the present work, we use the z bins as used in Yankelevich & Porciani (2019) and we also adopt their predicted values for the bias parameters b_1 and γ_2 , the survey volume V and the pairwise velocity dispersion σ_p . We have used the Boltzmann code CLASS (Lesgourgues 2011; Blas et al. 2011) to compute the real space matter power spectrum and the growth rate f for each z bin.

We have considered the $z = 0.7$ redshift bin as the fiducial value for which most of our results are shown. Following Yankelevich & Porciani (2019), we have adopted the values $b_1 = 1.18$, $\gamma_2 = -0.9$, $V = 8.97 \text{ Gpc}^3$ and $\sigma_p = 7.09 \text{ Mpc}$ for this particular z bin. Figure 2 shows Q_ℓ^m as functions of μ and t at $k_1 = 0.2 \text{ Mpc}^{-1}$ for the fiducial redshift $z = 0.7$. Here $k_1 = 0.2 \text{ Mpc}^{-1}$ is a sufficiently large length-scale where we may expect a combination of 2PT and FoG to provide a reasonably good description of the redshift space bispectrum. The cosmic variance is expected to increase if we consider small values of k_1 , whereas non-linear effects increase if we consider larger k_1 . Guided by this, we have mainly shown the results for $k_1 = 0.2 \text{ Mpc}^{-1}$. We now briefly discuss the shapes of the triangle corresponding to different values of μ and t , the reader is referred to Paper I for further details. Considering any panel of fig. 2, the right boundary $\mu = 1$ corresponds to linear triangles where the three sides are co-linear. Here, the bottom right corner $(\mu, t) = (1, 0.5)$ corresponds to stretched triangles where $k_2 = k_3 = k_1/2$, and the top right corner $(1, 1)$ corresponds to squeezed triangles where $k_1 = k_2, k_3 \rightarrow 0$. The top boundary $t = 1$ corresponds to L-isosceles triangles where the two larger sides have equal

length ($k_1 = k_2$), and the bottom boundary $2\mu t = 1$ corresponds to S-isosceles triangles where the two smaller sides have equal length ($k_2 = k_3$). The top left corner $(0.5, 1)$ corresponds to equilateral triangles. The diagonal $\mu = t$ corresponds to right-angled triangles, and the regions $t > \mu$ and $t < \mu$ correspond to acute and obtuse triangles respectively.

3.1 Predicted Multipole Moments

In fig. 2, we have shown Q_ℓ^m for $\ell = 0, 2$ and 4. As mentioned earlier, only the even ℓ multipoles are expected to be non-zero. Further, in 2PT we expect non-zero multipoles up to $\ell = 8$ (Paper II), however the value of Q_ℓ^m falls with increasing ℓ and m , and we have shown the main results only up to $\ell = 4, m = 3$. As shown later in this section, we do not expect to have a statistically significant measurement of the higher multipoles for the survey parameters considered here. Note that Q_ℓ^m and $Q_\ell^m[\text{FoG}]$ respectively denote the results without and with the FoG. In all cases we find that the magnitude of $Q_\ell^m[\text{FoG}]$ is highly suppressed compared to Q_ℓ^m due to the FoG effect. Considering Q_0^0 , we find that the the minima (0.33) occurs for the equilateral triangles and the the maxima (52.83) occurs close to the squeezed limit ($\mu \rightarrow 1, t = 0.865$). The minimum and maximum values fall to 0.09 and 23.50 for $Q_0^0[\text{FoG}]$. We notice that the drop in value due to the FoG is more pronounced for equilateral triangles where the minima occurs. However, the overall patterns are visually very similar for Q_ℓ^m and $Q_\ell^m[\text{FoG}]$.

The contour pattern of Q_2^0 shows features similar to those of Q_0^0 . Its peak value (86.83) is larger than the peak value of Q_0^0 and it occurs at $\mu = 0.995, t = 0.795$. We observe that the FoG effect causes a larger suppression for the quadrupole than in monopole, and the maximum value of $Q_2^0[\text{FoG}]$ drops to 11.95 which occurs at a slightly different location (at $\mu = 0.995, t = 0.735$). It is interesting to note that in the absence of the FoG damping Q_2^0 is larger than than all the other multipoles including the monopole. However as soon as we apply the FoG effect, the peak value of $Q_2^0[\text{FoG}]$ drops and $Q_0^0[\text{FoG}]$ overtakes it to become the multipole with the largest value. The entire contour pattern of $Q_2^0[\text{FoG}]$ is quite different from that of Q_2^0 . Unlike Q_2^0 which is positive everywhere, we see that $Q_2^0[\text{FoG}]$ is negative over a region near the squeezed limit. The minimum values of Q_2^0 (0.23) and $Q_2^0[\text{FoG}]$ (-3.88) respectively occurs at the equilateral and squeezed limits, however the magnitude of $Q_2^0[\text{FoG}]$ is still minimum for equilateral triangles.

Considering Q_2^1 , we find that this has negative values for most of the acute triangles and positive values for obtuse triangles, with a zero crossing somewhat above the line $\mu = t$ which corresponds to right-angled triangles. The minima (-0.43) and maxima (19.24) respectively occur at $(\mu = 0.965, t \rightarrow 1)$ and $(\mu \rightarrow 1, t = 0.915)$ which are both very close to the squeezed limit. The FoG effect substantially changes the contour pattern, and we see that $Q_2^1[\text{FoG}]$ is positive valued throughout. The maxima (9.61) now occurs near the squeezed limit while the minima (≈ 0) occurs for equilateral triangles.

In case of Q_2^2 , we find that the minimum value (0.08) is near the stretched limit and the maximum value (6.45) occurs close to the squeezed limit ($\mu \rightarrow 1, t = 0.975$). The maximum (4.84) and minimum (0.04) values in case of $Q_2^2[\text{FoG}]$ do not

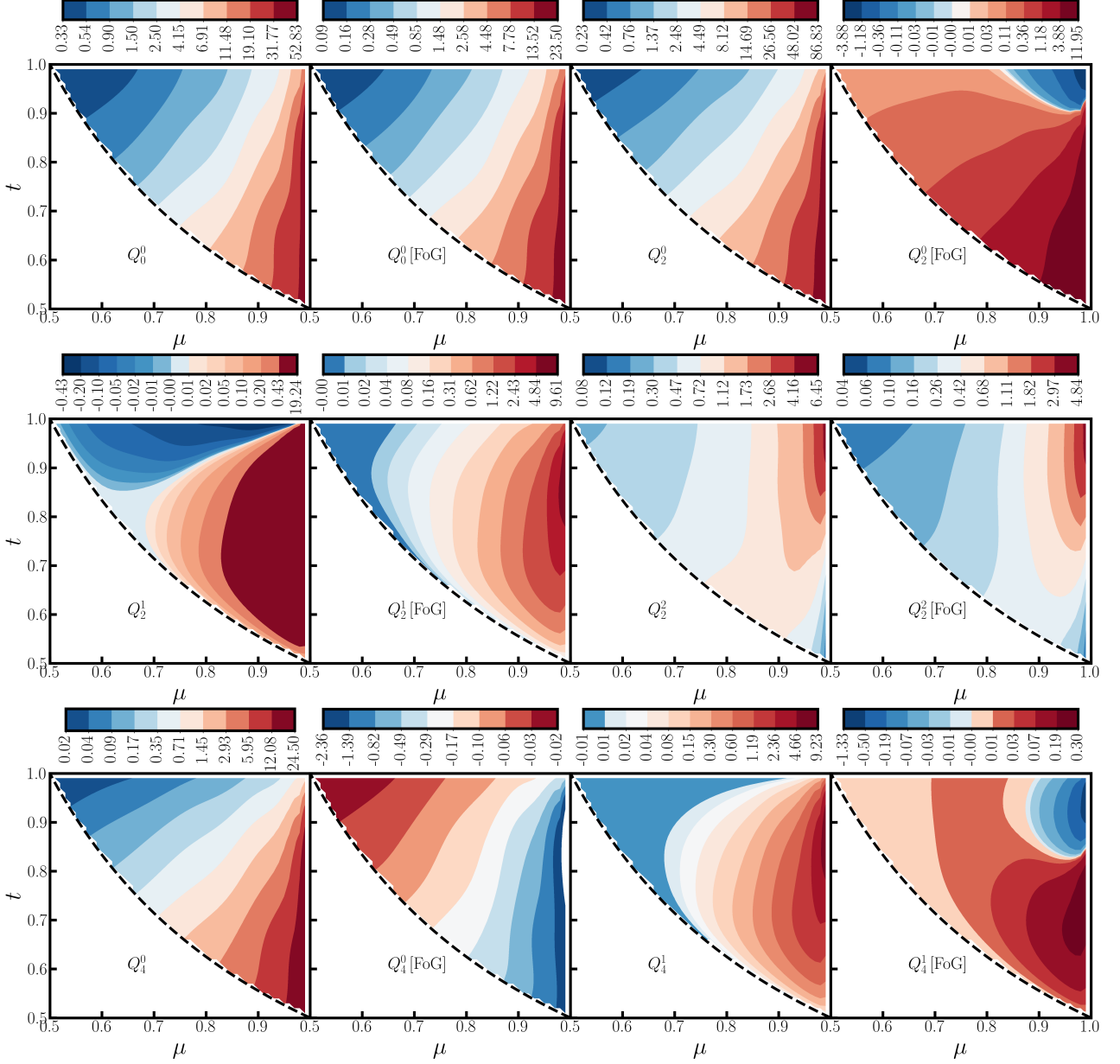


Figure 2. This shows Q_ℓ^m as functions of μ and t at $k_1 = 0.2\text{Mpc}^{-1}$ for the fiducial redshift $z = 0.7$. $Q_\ell^m[\text{FoG}]$ means that the effect of FoG has been considered in bispectrum according to eq. (30). In other plots, where FoG is not mentioned in the parenthesis, the bispectrum is considered only up to the 2PT level (eq. 25). From the plots it is evident that FoG suppress the bispectrum significantly at $k_1 = 0.2\text{Mpc}^{-1}$.

change position, only the amplitudes drop. Overall, Q_2^2 and $Q_2^2[\text{FoG}]$ show similar contour patterns.

Considering Q_4^0 , we see that it shows similar shape dependence as Q_0^0 and Q_2^0 , only its maximum (21.5) and minimum (0.02) values are smaller. Comparing $Q_4^0[\text{FoG}]$ with Q_4^0 , we see that the patterns are visually similar, however the values of $Q_4^0[\text{FoG}]$ are all negative and they are roughly an order of magnitude smaller. Considering Q_4^1 , we see that its minima (0.01) occurs for equilateral triangles and the maxima (9.23) is at $(\mu \rightarrow 1, t = 0.905)$ which is somewhat below the squeezed limit. Comparing $Q_4^1[\text{FoG}]$ with Q_4^1 , we see that the patterns are quite different, and the values of $Q_4^1[\text{FoG}]$ are

roughly an order of magnitude smaller. We see that $Q_4^1[\text{FoG}]$ is negative near the squeezed limit where $|Q_4^1|$ has a maxima (1.33), whereas the minima (0.30) occurs for equilateral triangles. In summary we note that the FoG effect has a significant impact on the redshift space bispectrum at the length-scales and redshifts of our interest, and we have included this in our subsequent analysis.

It is interesting to compare the Q_ℓ^m values (without FoG) shown in fig. 2 with those shown in Paper II. We note that the bias parameters and redshift $z = 0.7$ used here are different from those used in Paper II. We find that the contour patterns of Q_0^0, Q_2^0 and Q_4^0 look very similar in both fig. 2

and Paper II, however their values are ≥ 5 times larger in Paper II which considers $z = 0$. On the other hand, the odd multipoles are found to be very different. For example, in Paper II the minima and maxima of Q_2^1 lie along the $\mu = 1$ and $t = 1$ lines respectively whereas it is exactly the opposite in fig. 2. This is also true for Q_4^1 where the contour patterns show completely opposite trends in Paper II and fig. 2. These differences are mainly due to the choice of the non-linear bias parameter γ_2 which is set to zero in Paper II whereas we have used $\gamma_2 = -0.9$ for fig. 2.

The entire discussion has been restricted to $k_1 = 0.2\text{Mpc}^{-1}$ till now. It is worth noting that the impact of the FoG effect falls exponentially as we move to lower k (large scales), and it causes $\lesssim 5\%$ change in the bispectrum at $k_1 = 0.05\text{Mpc}^{-1}$ for $z = 0.7$. Second order perturbation theory (eq. 25) alone is adequate to model the redshift space bispectrum at $k_1 < 0.05\text{Mpc}^{-1}$, however we do not consider these small k_1 values in our work as most of the bispectrum multipoles become undetectable due to cosmic variance (as shown later).

3.2 SNR predictions

We now quantify the prospects of detecting the various bispectrum multipole moments B_ℓ^m using the signal-to-noise ratio (SNR) which is defined as

$$[\text{SNR}]_\ell^m = \frac{|B_\ell^m|}{\sqrt{C_\ell^{mm}}}. \quad (32)$$

A value $[\text{SNR}]_\ell^m \geq 5$ (or possibly $[\text{SNR}]_\ell^m \geq 3$) would be considered as a statistically significant detection of the particular multipole moment. As mentioned earlier, we have considered bins of width ($\Delta \ln k_1 = 0.1, \Delta \mu = 0.05, \Delta t = 0.05$). We note that the signal to noise ratio will increase if we consider bins of larger widths. Considering a situation where our analysis predicts $[\text{SNR}]_\ell^m \approx 1$, it may still be possible to achieve a statistically significant detection by widening the bin width using ($\Delta \ln k_1 = 0.2, \Delta \mu = 0.1, \Delta t = 0.1$) which still retains a significant amount of the information regarding the length-scale and shape dependence of the bispectrum. Further the values of the various parameters used in our predictions are rather uncertain, and it is possible that the actual parameter values could result in a larger $[\text{SNR}]_\ell^m$. Motivated by these factors, we have shown the results for $[\text{SNR}]_\ell^m \geq 1$ where the signal and noise have equal amplitude, and we have also included this in the discussion.

Figure 3 shows $[\text{SNR}]_\ell^m$ for different multipoles with $k_1 = 0.2\text{Mpc}^{-1}$ and $z = 0.7$ fixed. The regions where $[\text{SNR}]_\ell^m < 1$ have been masked out from the plots, and the multipoles where $[\text{SNR}]_\ell^m$ never exceeds unity have not been shown. Broadly, the $[\text{SNR}]_\ell^m$ values decrease with increasing ℓ , and for a fixed ℓ they decrease with increasing m . However, we find an exception that the maximum value of $[\text{SNR}]_2^1$ exceeds that of $[\text{SNR}]_2^0$. For all $[\text{SNR}]_\ell^m$ we find that the maximum value occurs for linear triangles ($\mu = 1$), however the value of t corresponding to the maxima varies depending on ℓ and m . Further, in most cases $[\text{SNR}]_\ell^m$ decreases as the shape of the triangle is changed from linear ($\mu = 1$) to other obtuse triangles ($\mu > t$) and then acute triangles ($\mu < t$) and finally the equilateral triangle ($\mu, t = (0.5, 1)$). Considering B_0^0 , we see that this can be detected at a high level of precision ($[\text{SNR}]_0^0 > 7$) for all triangle configurations, and $[\text{SNR}]_0^0$ is maximum (≈ 140) around $(1, 0.75)$. Considering B_2^0 , we see

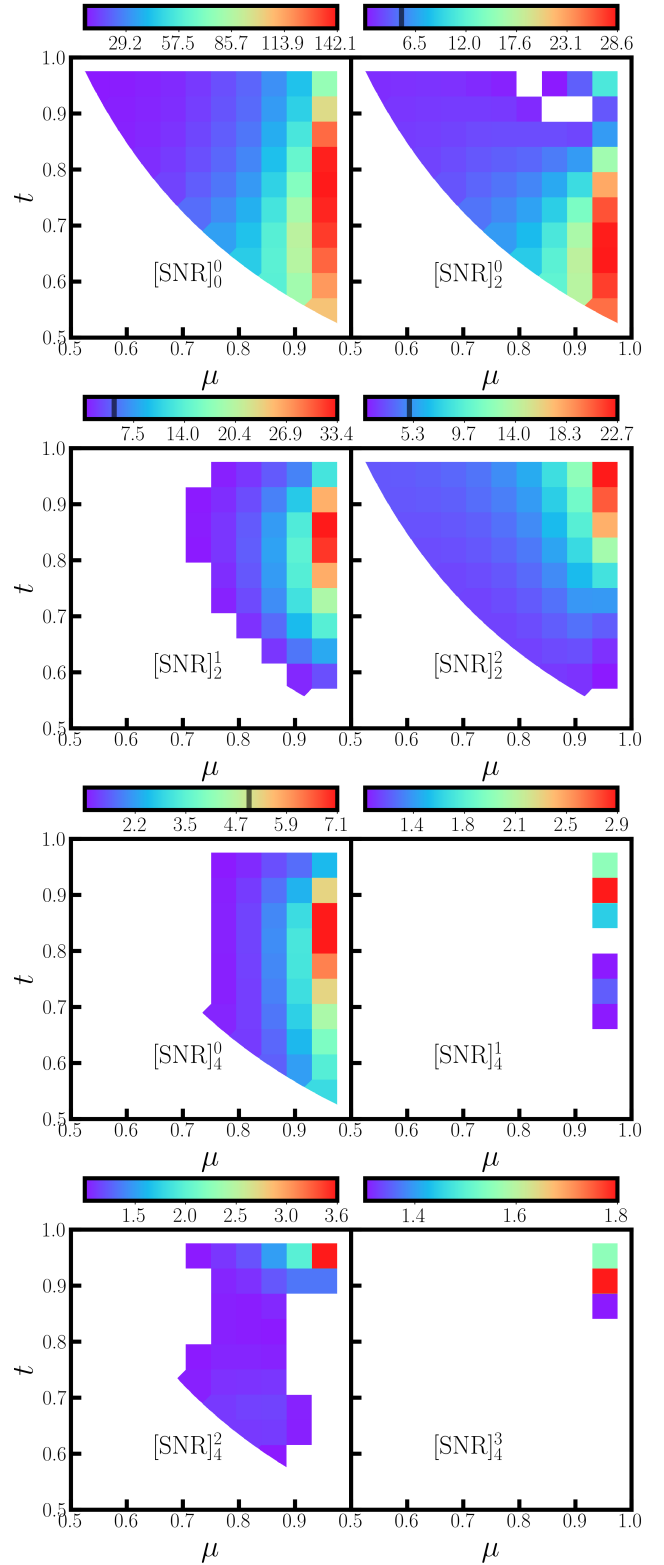


Figure 3. This shows the signal to noise $[\text{SNR}]_\ell^m$ (eq. 32) for different multipoles with $k_1 = 0.2\text{Mpc}^{-1}$ and $z = 0.7$ fixed. The regions where $[\text{SNR}]_\ell^m < 1$ have been masked out from the plots. We do not show the multipoles for which $[\text{SNR}]_\ell^m$ never exceeds unity. The vertical grey lines in the color bars mark the values $[\text{SNR}]_\ell^m = 5$.

that the SNR exceeds unity for most triangle configurations, however $[\text{SNR}]_2^0 < 5$ over a considerable region where $t > \mu$. We also find a small region with $[\text{SNR}]_2^0 < 1$ near the squeezed limit where the values of B_2^0 have a zero crossing (fig. 2). The maximum value $[\text{SNR}]_2^0 = 28.6$ occurs around $(1, 0.6)$ which is near the stretched limit. Considering $[\text{SNR}]_2^1$, we see that the maximum value (≈ 33.4) occurs around $(1, 0.85)$ and we have $[\text{SNR}]_2^1 > 5$ in a region surrounding this. As mentioned earlier, the maximum value of $[\text{SNR}]_2^1$ exceeds that of all the other multipole moments barring $[\text{SNR}]_0^0$, however the condition $[\text{SNR}]_2^1 > 1$ is satisfied for a relatively small range of shapes compared to $[\text{SNR}]_2^0$ and $[\text{SNR}]_2^2$. The maximum value of $[\text{SNR}]_2^2$ (≈ 22.7) occurs for squeezed triangles, and we have $[\text{SNR}]_2^2 > 5$ in a region around this. The condition $[\text{SNR}]_2^2 > 1$ is satisfied over most of the (μ, t) space except for a small region near the stretched limit. $[\text{SNR}]_4^0$ is very similar to $[\text{SNR}]_2^1$, except that the values are smaller and the maximum value now is ≈ 7.1 . The higher multipoles with $\ell = 4$ and $m = 1, 2$ and 3 do not have $[\text{SNR}]_\ell^m > 5$ anywhere, however there is a rather large region where $[\text{SNR}]_4^2 > 1$. The maxima of $[\text{SNR}]_4^2$ (≈ 3.6) occurs at the squeezed limit, whereas for $(m = 1, 3)$ the maxima $(2.9, 1.8)$ occur very close to the squeezed limit. The two latter multipoles satisfy $[\text{SNR}]_\ell^m > 1$ in only a small region around the maxima.

We now consider the k_1 dependence of $[\text{SNR}]_\ell^m$ with $z = 0.7$ fixed, as shown in fig. 4. The smallest value of k_1 roughly corresponds to the linear extent of the survey. The results are shown for only three different triangle shapes namely squeezed, stretched and equilateral. However, we can combine these with fig. 3 to qualitatively infer the k_1 dependence expected for other triangle configurations. The number of triangles in any bin scales as $N_{tr} \propto k_1^3$ (eq. 22), and we expect the cosmic variance to scale as k_1^{-3} (eq. 24) as k_1 is increased. Based on this we may expect $[\text{SNR}]_\ell^m$ to increase monotonically with increasing k_1 . This is broadly true for all the triangles in fig. 4, except for the sharp dips which are seen to occur for a few of the multipoles at certain values of k_1 . As seen in fig. 2, some of the multipoles have both positive and negative values, and the dips in fig. 4 correspond to the zero crossings which are also reflected in $[\text{SNR}]_\ell^m$. We now discuss the prospects of detecting the various multipoles at different values of k_1 . Here we use $k_1[5]$ to denote the smallest value of k_1 where the condition $[\text{SNR}]_\ell^m > 5$ is satisfied, and generally we expect the B_ℓ^m to be detectable for all $k_1 \geq k_1[5]$. Considering B_0^0 we see that $k_1[5] = 0.05\text{Mpc}^{-1}$ for the squeezed and stretched triangles, and $k_1[5] = 0.1\text{Mpc}^{-1}$ for equilateral triangles. Overall, we expect to detect B_0^0 for all linear triangles and some obtuse triangles at $k_1 \geq 0.05\text{Mpc}^{-1}$, and for all triangle at $k_1 \geq 0.1\text{Mpc}^{-1}$. Note that B_0^0 is predicted to be negative at large k_1 for equilateral triangles. We find a small k_1 range around $k_1 \approx 0.4\text{Mpc}^{-1}$ where we do not expect to detect B_0^0 for equilateral and possibly some of the acute triangles. Considering B_2^0 , we have $k_1[5] = 0.05\text{Mpc}^{-1}$ and 0.1Mpc^{-1} for stretched and squeezed triangles respectively. The SNR falls off towards equilateral triangles where we have $\text{SNR} \geq 1$ for $k_1 \geq 0.1\text{Mpc}^{-1}$ and $k_1[5] = 0.6\text{Mpc}^{-1}$. Overall we expect B_2^0 to be detectable in the vicinity of the stretched limit for $k_1 \geq 0.05\text{Mpc}^{-1}$, and for several other linear and obtuse triangles for $k_1 \geq 0.1\text{Mpc}^{-1}$. Considering acute and equilateral triangles, it will be possible to detect B_2^0 at $k_1 \geq 0.1\text{Mpc}^{-1}$ if we increase the bin widths. For all shapes, B_2^0 is predicted to be negative at large k_1 . The transi-

tion from positive to negative values occurs at $k_1 \approx 0.1\text{Mpc}^{-1}$ for squeezed triangles, and then spreads to other shapes (stretched and then equilateral) as k_1 is increased. As seen in fig. 3, it will not be possible to detect B_2^0 in a few $\mu - t$ bins where the zero crossing occurs. The exact $\mu - t$ locations of these bins will shift with k_1 . Considering B_2^1 and B_2^2 together, we see that $k_1[5] \approx 0.1\text{Mpc}^{-1}$ for squeezed triangles, and we expect to detect these multipoles for several linear and obtuse triangles for $k_1 \geq 0.1\text{Mpc}^{-1}$. Further, in all three cases (fig. 4) B_2^2 satisfies $\text{SNR} \geq 1$ for $k_1 > 0.1\text{Mpc}^{-1}$. In this k_1 range we expect to detect B_2^2 across the entire $\mu - t$ plane if we consider larger bin widths. We find that the rest of B_ℓ^m shown here ($\ell = 4, m = 0, 1, 2, 3$) all have $k_1[5]$ in the range $0.2 - 0.3\text{Mpc}^{-1}$ for squeezed triangles, and we expect to detect these multipoles for several linear and obtuse triangles near the squeezed limit. We note that B_4^0 also has $k_1[5]$ in the range $0.2 - 0.3\text{Mpc}^{-1}$ for stretched triangles, and the region of $\mu - t$ space where this will be detected is relative large compared to the other $\ell = 4$ multipoles. We also note that B_4^0 and B_4^2 both satisfy $\text{SNR} \geq 1$ for the three triangle shapes shown in fig. 4 for $k_1 \geq 0.3\text{Mpc}^{-1}$, and we expect to detect these over the entire $\mu - t$ space if we increase the bin widths.

Figure 5 shows how $[\text{SNR}]_\ell^m$ varies with redshift with $k_1 = 0.2\text{Mpc}^{-1}$ fixed. Note that the bias parameters b_1, γ_2 , as well as the survey volume V change with changing redshift, and we have used the redshift dependent values from Table 1 of (Yankelevich & Porciani 2019). We see that the survey volume V increases with z , and we expect the cosmic variance at a fixed k_1 to decrease with increasing z . As a result of this, $[\text{SNR}]_\ell^m$ is expected to increase monotonically with redshift. However, there are two more effects that determine $[\text{SNR}]_\ell^m$ values at each z : (i) the amplitude of the bispectrum decreases with increasing z , and (ii) the FoG suppression also decreases with increasing z . The bias parameters also affect the z dependence of $[\text{SNR}]_\ell^m$. We see that for many of the multipoles $[\text{SNR}]_\ell^m$ increase slightly with increasing z whereas there are some where the opposite occurs, and for a few cases we also have dips in $[\text{SNR}]_\ell^m$ at some values of z . As discussed earlier, these dips correspond to the zero crossings of B_ℓ^m . We now discuss the prospects of detecting the different multipoles at the various redshifts shown here. Considering B_0^0 , we see that this is detectable with $[\text{SNR}]_0^0 > 5$ at all the redshifts for all the three triangles considered. B_2^0 is detectable with $[\text{SNR}]_2^0 > 5$ at all redshifts for stretched triangles. For squeezed triangles, the above is true for $z < 1.5$, whereas for equilateral triangles $1 < [\text{SNR}]_2^0 < 5$ at all redshifts. Considering B_2^1 and B_2^2 , we see that they will be detected with $[\text{SNR}]_\ell^m > 5$ at all the redshifts only for squeezed triangles. For the stretched and equilateral triangles, $[\text{SNR}]_2^1$ and $[\text{SNR}]_2^2$ values are below 5 at all redshifts. All the $\ell > 2$ multipoles cannot be observed with $[\text{SNR}]_\ell^m > 5$ at any redshift and for the triangle shapes considered. Note that, the above discussion is true only for for three specific triangle shapes at $k_1 = 0.2\text{Mpc}^{-1}$. However, as we have discussed earlier, it is possible to detect the higher order multipoles with $[\text{SNR}]_\ell^m > 5$ by considering triangles of other shapes or somewhat larger k_1 values or larger bin widths.

3.3 Correlation between different multipoles

It is important to note that the estimated values of the different multipole moments are expected to be correlated. We

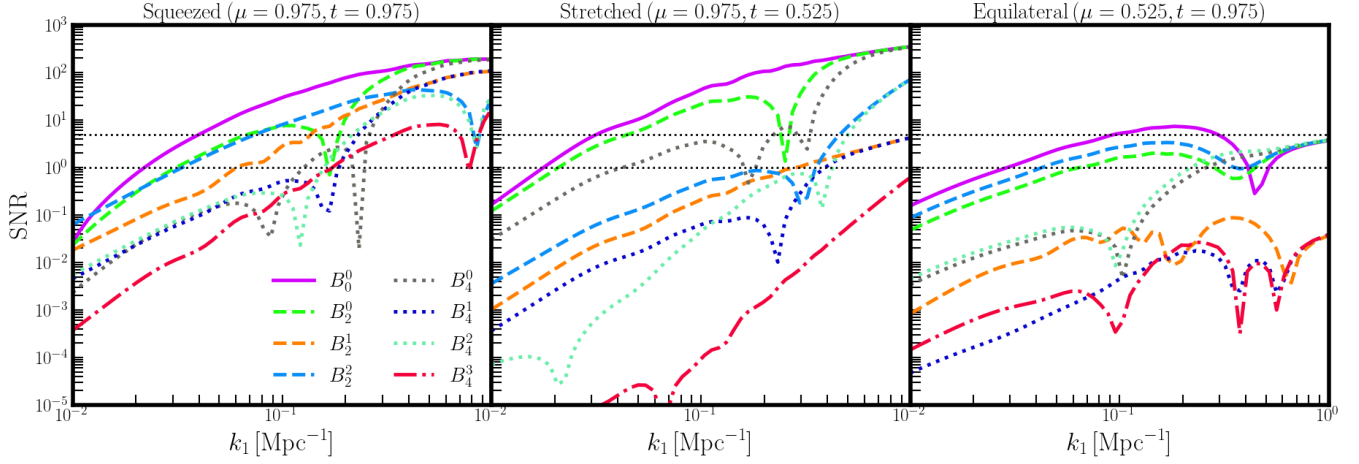


Figure 4. This shows the variation of $[\text{SNR}]_\ell^m$ (eq. 32) with k_1 , the largest wavevector (see fig. 1), at fixed $z = 0.7$. We show results for three specific triangle shapes: **squeezed** (left-hand panel), **stretched** (central panel) and **equilateral** (right-hand panel). The horizontal dotted-black lines show the $[\text{SNR}]_\ell^m = 1$ and 5 levels respectively. Note that we show $[\text{SNR}]_\ell^m$ for the same multipoles as in fig. 3.

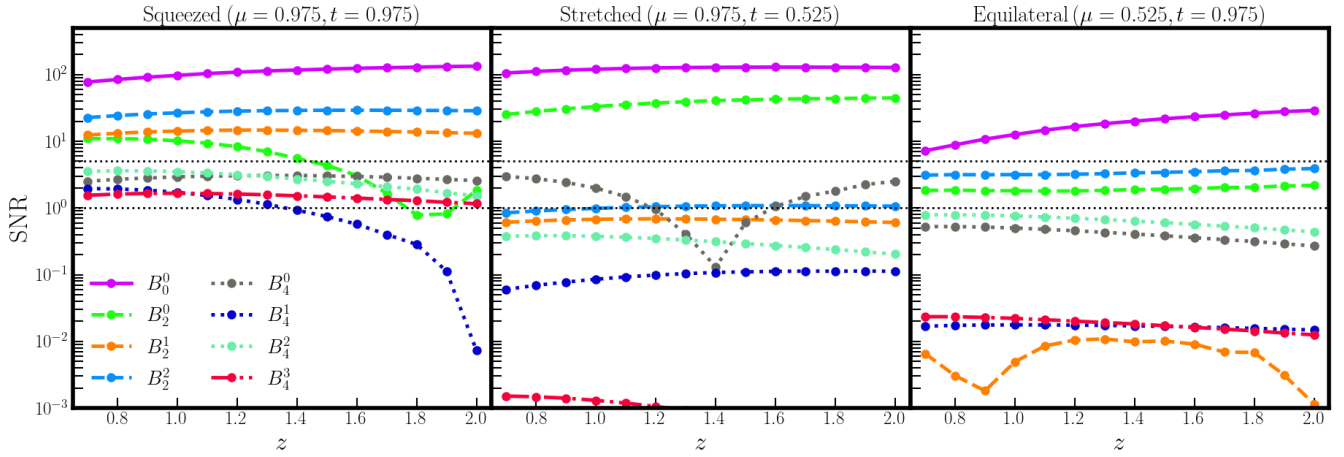


Figure 5. This shows the variation of $[\text{SNR}]_\ell^m$ (eq. 32) with redshift at fixed $k_1 = 0.2 \text{ Mpc}^{-1}$. We show results for three specific triangle shapes: **squeezed** (left-hand panel), **stretched** (central panel) and **equilateral** (right-hand panel). The horizontal dotted-black lines show the $[\text{SNR}]_\ell^m = 1$ and 5 levels respectively. Note that we show $[\text{SNR}]_\ell^m$ for the same multipoles as in fig. 3. Filled circles represent the z bins adopted from Yankelevich & Porciani (2019) to show our results.

have quantified the correlations in the measurement errors between any two multipoles using the rank correlation

$$\mathcal{R}_{\ell\ell'}^{mm'} = \frac{C_{\ell\ell'}^{mm'}}{\sqrt{C_{\ell\ell}^{mm}} \sqrt{C_{\ell'\ell'}^{m'm'}}}. \quad (33)$$

with $-1 \leq \mathcal{R}_{\ell\ell'}^{mm'} \leq 1$. Here positive and negative values indicate that the errors are correlated and anti-correlated respectively. We show the rank correlations between different multipoles in fig. 6. We find that for most multipole pairs, the errors are only weakly correlated ($|\mathcal{R}_{\ell\ell'}^{mm'}| < 0.1$) across much of the $\mu - t$ plane. However, there are a few exceptions which we highlight below. We first consider \mathcal{R}_{02}^{00} which refers to B_0^0 and B_2^0 which have the highest SNR. We see that the measurement errors in these two multipoles are correlated for obtuse triangles and anti-correlated for acute trian-

gles. \mathcal{R}_{02}^{00} shows the highest correlation (0.42) in the stretched limit, and the highest anti-correlation (-0.1) in the squeezed limit. Considering \mathcal{R}_{02}^{02} , we see that the measurement errors of the pair (B_0^0, B_2^2) are correlated with values ~ 0.25 in the vicinity of the squeezed limit. Considering \mathcal{R}_{22}^{02} , we see that this show maximum anti-correlation (-0.18) in the stretched limit. \mathcal{R}_{24}^{00} shows the highest correlation (0.33) and anti-correlation (-0.1) in the stretched and squeezed limits respectively. We have $|\mathcal{R}_{\ell\ell'}^{mm'}| < 0.1$ across the entire $\mu - t$ plane for all the other multipoles not shown here. Overall, the errors in the various multipoles are weakly correlated for most triangle shapes barring a few in the vicinity of squeezed and stretched triangles.

Figure 7 shows the redshift dependence (from $z = 0.7$ to 2) of the four rank correlations shown in fig. 6 for three specific triangle shapes with $k_1 = 0.2 \text{ Mpc}^{-1}$ fixed. Considering

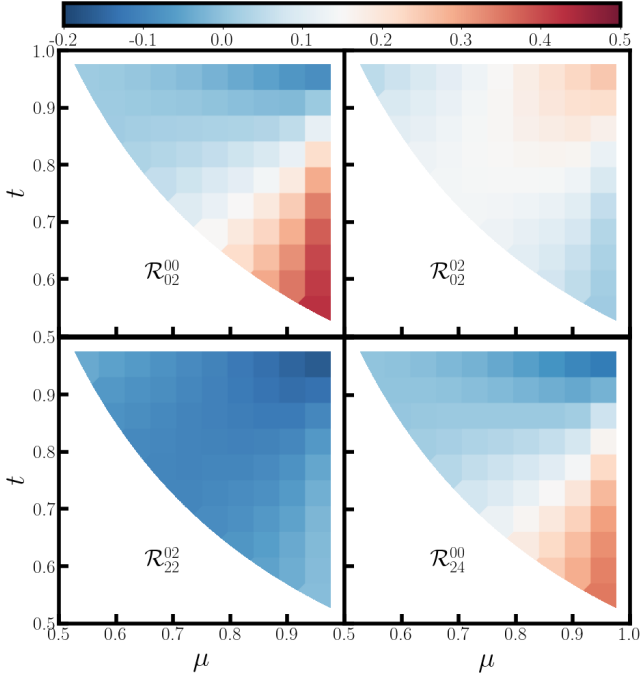


Figure 6. This shows rank correlations $\mathcal{R}_{\ell\ell'}^{mm'}$ (eq. 33) between different multipoles at fixed $k_1 = 0.2 \text{Mpc}^{-1}$ and $z = 0.7$. Note that, we do not show rank correlations for which $|\mathcal{R}_{\ell\ell'}^{mm'}| < 0.1$ throughout the $\mu - t$ plane.

\mathcal{R}_{02}^{00} (\mathcal{R}_{24}^{00}) we see that the peak correlation, which occurs for stretched triangles, increases from 0.42 (0.32) to ~ 0.5 (0.4) whereas the value changes from ~ -0.1 to ~ 0.1 for squeezed triangles. Considering \mathcal{R}_{02}^{02} , the peak correlation, which occurs for squeezed triangles, drops from ~ 0.25 to 0.2 across z . Considering \mathcal{R}_{22}^{02} , for squeezed triangles its value changes from -0.18 to -0.11 across z . The other cases shown in the figure all have $|\mathcal{R}_{\ell\ell'}^{mm'}| < 0.1$, with the exception of \mathcal{R}_{02}^{02} which has values in the range 0.1 to 0.2 at $z \geq 1$ for equilateral triangles.

Figure 8 shows the k_1 dependence of the four rank correlations shown in fig. 6 for three specific triangle shapes with $z = 0.7$ fixed. Considering all the panels, we see that the rank correlations are practically independent of k_1 for $k_1 \lesssim 0.05 \text{Mpc}^{-1}$. We have already mentioned that the FoG effect can be neglected at $k_1 \lesssim 0.05 \text{Mpc}^{-1}$. The numerator and denominator of eq. (33) are both dominated by the power spectrum contribution, and the k_1 dependent factors cancel out to make $\mathcal{R}_{\ell\ell'}^{mm'}$ independent of k_1 in the absence of the FoG effect. However, we see a strong k_1 dependence for $k_1 > 0.1 \text{Mpc}^{-1}$ where the FoG is important. We see that \mathcal{R}_{02}^{00} and \mathcal{R}_{24}^{00} exhibit very similar k_1 dependence in all the three panels where we have positive correlations at $k_1 < 0.05 \text{Mpc}^{-1}$, the correlations decline with increasing k_1 and cross zero around $k_1 \sim 0.2$ and we have nearly complete anti-correlation (~ -1) for $k_1 > 0.5 \text{Mpc}^{-1}$. Considering $k_1 < 0.05 \text{Mpc}^{-1}$ we have $\mathcal{R}_{02}^{00} > \mathcal{R}_{24}^{00}$, with the maximum correlation (0.5 – 0.75) occurring for stretched triangles, followed by values in the range 0.3 – 0.5 for squeezed triangles and 0.2 – 0.3 for equilateral triangles. The k_1 dependence of \mathcal{R}_{02}^{02} is very similar to that of \mathcal{R}_{02}^{00} and \mathcal{R}_{24}^{00} for equilateral

triangles. For squeezed (stretched) triangles $\mathcal{R}_{02}^{02} \sim 0.25$ (0.0) for $k_1 \leq 0.4 \text{Mpc}^{-1}$ beyond which both sharply declines to ~ -0.25 at $k_1 = 1 \text{Mpc}^{-1}$. In contrast, \mathcal{R}_{22}^{02} shows exactly the opposite k_1 dependence in that we have anti-correlations for small k_1 and correlations at large k_1 , with a zero crossing whose k_1 value depends on the shape of the triangle. Considering squeezed, stretched and equilateral triangles we respectively have $\mathcal{R}_{22}^{02} \sim -0.1, 0.0$ and -0.2 at small k_1 ($\leq 0.1 \text{Mpc}^{-1}$), whereas these values are $\sim 0.25, 0.25$ and 1.0 for large k_1 ($\leq 0.1 \text{Mpc}^{-1}$).

4 DISCUSSION AND CONCLUSION

The redshift space anisotropy of the bispectrum is generally quantified using multipole moments as defined in eq. (6). The possibility of measuring these multipoles in any survey depends on the level of statistical fluctuations. In this paper, we developed a formalism to compute the statistical fluctuations in the measurement of bispectrum multipoles for galaxy surveys. We quantify the fluctuations through the covariance as defined in eq. (24) which assumes the flat sky approximation. We consider the specifications of a *Euclid* like galaxy survey to present our results. We mainly consider two quantities: (i) the signal-to-noise ratio (SNR) $[\text{SNR}]_{\ell}^m$ which quantifies the detectability of a multipole B_{ℓ}^m (eq. 32), and (ii) the rank correlation which quantifies the correlation in measurement errors between any two multipoles (eq. 33). We show, how these quantities depend on the triangle configurations in \mathbf{k} space, as well as their evolution in redshift. We also show how our results change as we introduce the FoG effect.

We find that the FoG effect plays a crucial role at length scales $k > 0.05 \text{Mpc}^{-1}$ for $z = 0.7$. This suppresses the values of bispectrum multipoles and the suppression is in general stronger for the higher order multipoles. The amplitude of the monopole B_0^0 predicted by 2PT is reduced by half when FoG effect is introduced. For B_4^m , the amplitude is suppressed by almost an order of magnitude in presence of FoG effect. This FoG suppression, however, is not very important at small k or at high z .

We see that in general $[\text{SNR}]_{\ell}^m$ values decrease with increasing ℓ , and for a fixed ℓ they decrease with increasing m . Considering all $[\text{SNR}]_{\ell}^m$, we find that the maximum value occurs for linear triangles ($\mu = 1$), however the value of t corresponding to the maxima varies depending on ℓ and m . Also, in most of the cases $[\text{SNR}]_{\ell}^m$ decreases as the shape of the triangle is changed from linear ($\mu = 1$) to other obtuse triangles ($\mu > t$) and then acute triangles ($\mu < t$) and finally the equilateral triangle ($\mu, t = (0.5, 1)$). We note that, at large, $[\text{SNR}]_{\ell}^m$ increases with k_1 and z .

Considering individual multipoles, we expect to detect B_0^0 for all the triangles at $k_1 > 0.1 \text{Mpc}^{-1}$ across the redshifts considered here. On the other hand, we expect B_2^0 to be detectable in the vicinity of the stretched limit for $k_1 > 0.05 \text{Mpc}^{-1}$ at all the redshifts, and for several other linear and obtuse triangles for $k_1 \geq 0.1$ up to $z \sim 1.5$. Detection of B_2^0 for acute and equilateral triangles, as well as for obtuse triangles at $z > 1.5$, is possible if we increase the bin size. Detection of B_2^2 and B_2^1 at all redshifts is possible only for squeezed triangles at $k_1 \geq 0.1 \text{Mpc}^{-1}$. For other triangle shapes, detection is possible at higher k_1 . Considering B_4^m multipoles, we see that the detection is possible across the

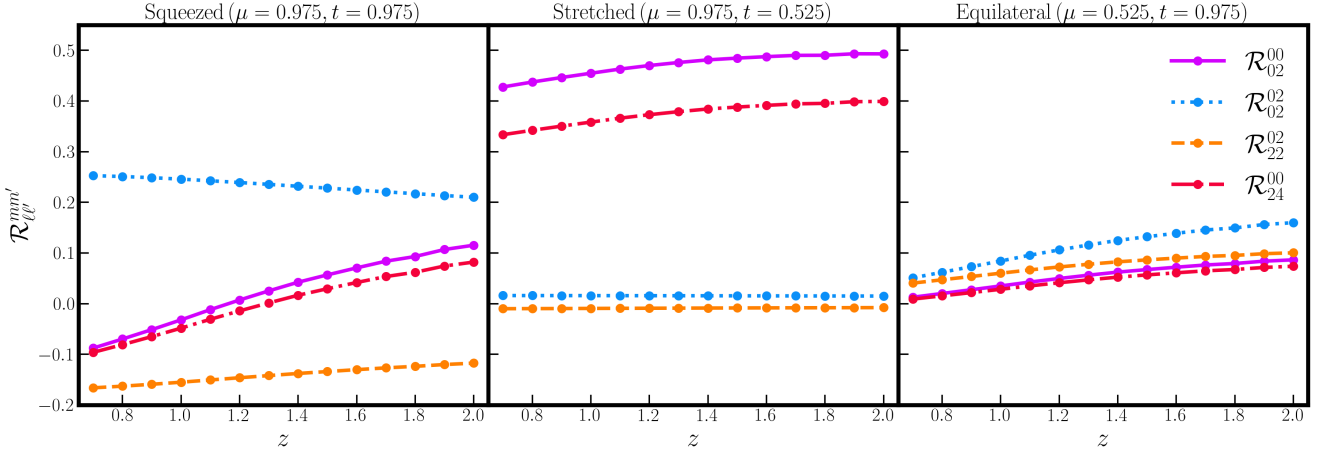


Figure 7. This shows the redshift dependence of the rank correlations $\mathcal{R}_{\ell\ell'}^{mm'}$ (eq. 33) between different multipoles for a fixed $k_1 = 0.2 \text{ Mpc}^{-1}$. We show results for three specific triangle shapes: **squeezed** (left-hand panel), **stretched** (central panel) and **equilateral** (right-hand panel). Note that, we have considered the same rank correlations as shown in fig. 6. Filled circles represent the z bins adopted from Yankelevich & Porciani (2019) to show our results.

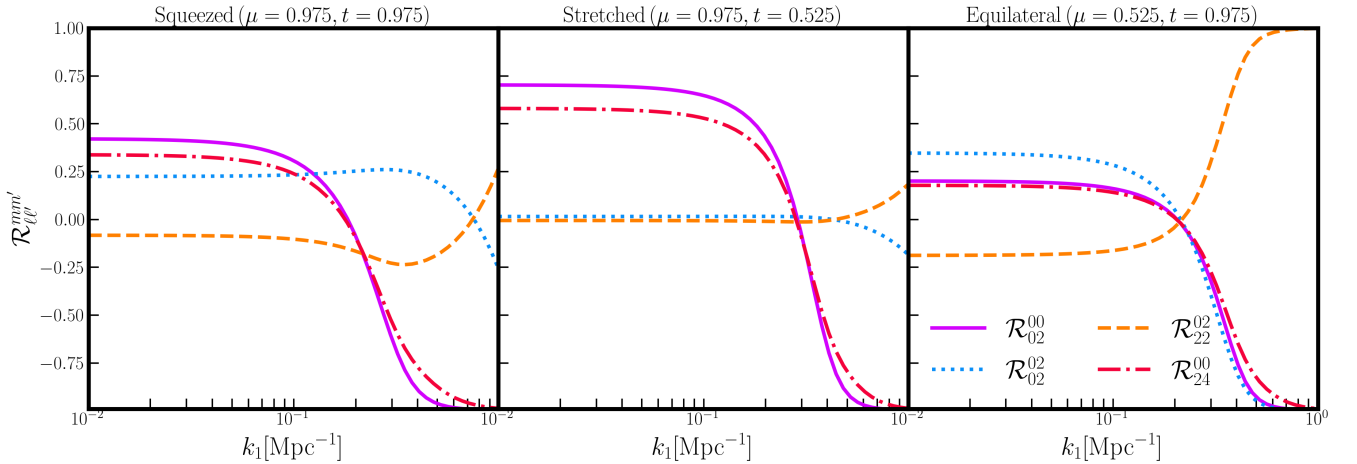


Figure 8. This shows the k_1 dependence of the rank correlations $\mathcal{R}_{\ell\ell'}^{mm'}$ (eq. 33) between different multipoles for a fixed $z = 0.7$. We show results for three specific triangle shapes: **squeezed** (left-hand panel), **stretched** (central panel) and **equilateral** (right-hand panel). Note that, we have considered the same rank correlations as shown in fig. 6.

redshift range only for a few linear and obtuse triangles near the squeezed limit at $k_1 > 0.2 \text{ Mpc}^{-1}$. Note that, for all the multipoles, the possibility of detection, or the $[\text{SNR}]_{\ell}^m$ values, can be increased by increasing the bin size in k_1, μ or t .

Considering $\mathcal{R}_{\ell\ell'}^{mm'}$, we find that for most multipole pairs the errors are only weakly correlated (with $|\mathcal{R}_{\ell\ell'}^{mm'}| < 0.1$) across much of the $\mu - t$ plane barring a few in the vicinity of squeezed and stretched triangles. For a fixed triangle shape, the $\mathcal{R}_{\ell\ell'}^{mm'}$ values are practically independent of k_1 for $k_1 \lesssim 0.05 \text{ Mpc}^{-1}$ and show a strong k_1 dependence for $k_1 > 0.1 \text{ Mpc}^{-1}$ where FoG effect is really important. For a fixed triangle shape and k_1 , $\mathcal{R}_{\ell\ell'}^{mm'}$ evolve moderately with redshift.

We, therefore, conclude that the future surveys like *Euclid* can potentially measure the higher order redshift space bispectrum multipoles (up to $\ell = 4$), beyond the isotropic

component (monopole), across various triangle shapes and sizes. The signal-to-noise or significance of these measurements, however, depend on the scales and redshifts of observation. The signal-to-noise also determines the information content of the individual multipoles. Significant measurements of $\ell \leq 2$ multipoles are possible even at $k_1 \lesssim 0.1 \text{ Mpc}^{-1}$ across the z range $0.7 - 2$. These scales are particularly important as the FoG suppression is minimum here. Here, we expect to measure the $\ell \leq 2$ multipoles with highest signal-to-noise for linear and obtuse triangles. For $\ell > 2$ multipoles, we require to go to large k_1 for significant detection or we need large bin size to increase the signal-to-noise. Due to the weak correlation (at $k_1 < 0.2 \text{ Mpc}^{-1}$) between the errors of multipole pairs for most of the triangle shapes, it is possible to combine different multipoles to increase the information content. This becomes particularly important when we try to

extract cosmological parameters from bispectrum measurements. Following our analysis, we expect to reduce the errors on the cosmological parameters when we combine the higher multipoles along with the monopole results (Gil-Marín et al. 2015, 2017; Philcox & Ivanov 2022). This we plan to study in future. Finally, we reiterate that in *Euclid* like surveys, we expect to measure bispectrum multipoles up to $\ell = 4$ by suitably choosing the scale and redshifts of observation.

DATA AVAILABILITY

The data generated during this work will be made available upon reasonable request to the authors.

REFERENCES

- Agarwal N., Desjacques V., Jeong D., Schmidt F., 2021, *JCAP*, 03, 021
- Akrami Y., et al., 2020, *Astron. Astrophys.*, 641, A9
- Ballardini M., Matthewson W. L., Maartens R., 2019, arXiv e-prints, p. [arXiv:1906.04730](https://arxiv.org/abs/1906.04730)
- Bartolo N., Komatsu E., Matarrese S., Riotto A., 2004, *Phys. Rep.*, 402, 103
- Baumann D., 2009, arXiv e-prints, p. [arXiv:0907.5424](https://arxiv.org/abs/0907.5424)
- Bernardeau F., Colombi S., Gaztanaga E., Scoccimarro R., 2002, *Phys. Rept.*, 367, 1
- Bharadwaj S., 2001, *MNRAS*, 327, 577
- Bharadwaj S., Mazumdar A., Sarkar D., 2020, *Mon. Not. Roy. Astron. Soc.*, 493, 594
- Blanchard A., et al., 2020, *Astron. Astrophys.*, 642, A191
- Blas D., Lesgourgues J., Tram T., 2011, *JCAP*, 07, 034
- Bose B., Byun J., Lacasa F., Moradinezhad Dizgah A., Lombriser L., 2020, *JCAP*, 02, 025
- Chudaykin A., Ivanov M. M., 2019, *JCAP*, 11, 034
- Clarkson C., de Weerd E. M., Jolicoeur S., Maartens R., Umeh O., 2019, *Mon. Not. Roy. Astron. Soc.*, 486, L101
- Croton D. J., et al., 2004, *Mon. Not. Roy. Astron. Soc.*, 352, 1232
- Dai J.-P., Xia J.-Q., 2020, *Mon. Not. Roy. Astron. Soc.*, 491, L61
- Davis M., Peebles P. J. E., 1982, *Astrophys. J.*, 267, 465
- Desjacques V., Jeong D., Schmidt F., 2018, *J. Cosmology Astropart. Phys.*, 2018, 035
- Fedeli C., Carbone C., Moscardini L., Cimatti A., 2011, *Mon. Not. Roy. Astron. Soc.*, 414, 1545
- Feldman H. A., Frieman J. A., Fry J. N., Scoccimarro R., 2001, *Physical Review Letters*, 86, 1434
- Fergusson J. R., Liguori M., Shellard E. P. S., 2012, *J. Cosmology Astropart. Phys.*, 2012, 032
- Fry J. N., 1984, *ApJ*, 279, 499
- Gaztanaga E., Cabre A., Castander F., Crocce M., Fosalba P., 2009, *Mon. Not. Roy. Astron. Soc.*, 399, 801
- Gil-Marín H., Noreña J., Verde L., Percival W. J., Wagner C., Manera M., Schneider D. P., 2015, *Mon. Not. Roy. Astron. Soc.*, 451, 539
- Gil-Marín H., Percival W. J., Verde L., Brownstein J. R., Chuang C.-H., Kitaura F.-S., Rodríguez-Torres S. A., Olmstead M. D., 2017, *Mon. Not. Roy. Astron. Soc.*, 465, 1757
- Gualdi D., Verde L., 2020, *JCAP*, 06, 041
- Guzzo L., et al., 2008, *Nature*, 451, 541
- Hahn C., Villaescusa-Navarro F., 2021, *JCAP*, 04, 029
- Hamilton A. J. S., 1997, in Ringberg Workshop on Large Scale Structure. ([arXiv:astro-ph/9708102](https://arxiv.org/abs/astro-ph/9708102)), doi:10.1007/978-94-011-4960-0_17
- Hamilton A. J. S., 1998, in Hamilton D., ed., *Astrophysics and Space Science Library* Vol. 231, The Evolving Universe. p. 185 ([arXiv:astro-ph/9708102](https://arxiv.org/abs/astro-ph/9708102)), doi:10.1007/978-94-011-4960-0_17
- Hashimoto I., Rasera Y., Taruya A., 2017, *Phys. Rev. D*, 96, 043526
- Hatton S. J., Cole S., 1999, *Mon. Not. Roy. Astron. Soc.*, 310, 1137
- Hawkins E., et al., 2003, *MNRAS*, 346, 78
- Hikage C., Yamamoto K., 2013, *J. Cosmology Astropart. Phys.*, 2013, 019
- Hikage C., Yamamoto K., 2016, *MNRAS*, 455, L77
- Hikage C., Mandelbaum R., Takada M., Spergel D. N., 2013, *MNRAS*, 435, 2345
- Hivon E., Bouchet F. R., Colombi S., Juszkiewicz R., 1995, *A&A*, 298, 643
- Hu W., Eisenstein D. J., Tegmark M., 1998, *Phys. Rev. Lett.*, 80, 5255
- Ilić S., et al., 2021
- Jackson J. C., 1972, *MNRAS*, 156, 1P
- Jing Y. P., Boerner G., 2004, *Astrophys. J.*, 607, 140
- Johnson A., Blake C., Dossett J., Koda J., Parkinson D., Joudaki S., 2016, *MNRAS*, 458, 2725
- Kaiser N., 1987, *MNRAS*, 227, 1
- Kulkarni G. V., Nichol R. C., Sheth R. K., Seo H.-J., Eisenstein D. J., Gray A., 2007, *Mon. Not. Roy. Astron. Soc.*, 378, 1196
- Laureijs R., et al., 2011, arXiv e-prints, p. [arXiv:1110.3193](https://arxiv.org/abs/1110.3193)
- Lesgourgues J., 2011, arXiv e-prints, p. [arXiv:1104.2932](https://arxiv.org/abs/1104.2932)
- Liguori M., Sefusatti E., Fergusson J. R., Shellard E. P. S., 2010, *Advances in Astronomy*, 2010, 980523
- Linder E. V., 2008, *Astroparticle Physics*, 29, 336
- Loveday J., Efstathiou G., Maddox S. J., Peterson B. A., 1996, *ApJ*, 468, 1
- Marín F., 2011, *Astrophys. J.*, 737, 97
- Matarrese S., Verde L., Heavens A. F., 1997, *MNRAS*, 290, 651
- Mazumdar A., Bharadwaj S., Sarkar D., 2020, *Mon. Not. Roy. Astron. Soc.*, 498, 3975
- Mueller E.-M., Percival W., Linder E., Alam S., Zhao G.-B., Sánchez A. G., Beutler F., Brinkmann J., 2018, *MNRAS*, 475, 2122
- Nan Y., Yamamoto K., Hikage C., 2018, *J. Cosmology Astropart. Phys.*, 2018, 038
- Nishimichi T., Kayo I., Hikage C., Yahata K., Taruya A., Jing Y. P., Sheth R. K., Suto Y., 2007, *PASJ*, 59, 93
- Okumura T., Hand N., Seljak U., Vlah Z., Desjacques V., 2015, *Phys. Rev. D*, 92, 103516
- Oppizzi F., Liguori M., Renzi A., Arroja F., Bartolo N., 2018, *J. Cosmology Astropart. Phys.*, 2018, 045
- Peacock J. A., 1992, in Martínez V. J., Portilla M., Sáez D., eds, *New Insights into the Universe*. Springer Berlin Heidelberg, Berlin, Heidelberg, pp 1–64
- Peacock J. A., et al., 2001, *Nature*, 410, 169
- Pearson D. W., Samushia L., 2018, *Mon. Not. Roy. Astron. Soc.*, 478, 4500
- Peebles P. J. E., 1980, The large-scale structure of the universe
- Philcox O. H. E., Ivanov M. M., 2022, *Phys. Rev. D*, 105, 043517
- Planck Collaboration et al., 2016, *A&A*, 594, A13
- Pozzetti L., et al., 2016, *Astron. Astrophys.*, 590, A3
- Sakurai J. J., 1994, *Modern quantum mechanics*; rev. ed.. Addison-Wesley, Reading, MA, <https://cds.cern.ch/record/1167961>
- Sarkar D., Bharadwaj S., 2018, *Mon. Not. Roy. Astron. Soc.*, 476, 96
- Sarkar D., Bharadwaj S., 2019, *Mon. Not. Roy. Astron. Soc.*, 487, 5666
- Scoccimarro R., 2004, *Phys. Rev. D*, 70, 083007
- Scoccimarro R., Couchman H. M. P., Frieman J. A., 1999, *Astrophys. J.*, 517, 531
- Scoccimarro R., Feldman H. A., Fry J. N., Frieman J. A., 2001, *Astrophys. J.*, 546, 652
- Scoccimarro R., Sefusatti E., Zaldarriaga M., 2004, *Phys. Rev. D*, 69, 103513

- Seljak U., 2001, *Mon. Not. Roy. Astron. Soc.*, 325, 1359
- Shiraishi M., 2019, *Frontiers in Astronomy and Space Sciences*, 6, 49
- Slepian Z., Eisenstein D. J., 2017, *Mon. Not. Roy. Astron. Soc.*, 469, 2059
- Slepian Z., Eisenstein D. J., 2018, *MNRAS*, 478, 1468
- Smith R. E., 2009, *MNRAS*, 400, 851
- Song Y.-S., Percival W. J., 2009, *J. Cosmology Astropart. Phys.*, 2009, 004
- Sugiyama N. S., Saito S., Beutler F., Seo H.-J., 2019, *MNRAS*, 484, 364
- Upadhye A., 2019, *JCAP*, 05, 041
- Verde L., Heavens A. F., Matarrese S., Moscardini L., 1998, *MNRAS*, 300, 747
- Verde L., et al., 2002, *MNRAS*, 335, 432
- White M. J., 2001, *Mon. Not. Roy. Astron. Soc.*, 321, 1
- Yankelevich V., Porciani C., 2019, *Mon. Not. Roy. Astron. Soc.*, 483, 2078
- de Weerd E. M., Clarkson C., Jolicoeur S., Maartens R., Umeh O., 2020, *JCAP*, 05, 018
- de la Torre S., et al., 2017, *Astron. Astrophys.*, 608, A44